Aalto University

Otero Fumega, Adolfo; Niedermeier, Marcel; Lado, Jose

Correlated states in super-moiré materials with a kernel polynomial quantics tensor cross interpolation algorithm

Correlated states in super-moiré materials with a kernel polynomial quantics tensor cross interpolation algorithm

To cite this article: Adolfo O Fumega *et al* 2025 *2D Mater.* **12** 015018

View the article online for updates and enhancements.

You may also like

- Emergent phases in graphene flat bands
  Saisab Bhowmik, Arindam Ghosh and U Chandni

- Indexing moiré patterns of metal-supported graphene and related systems: strategies and pitfalls
  Patrick Zeller, Xinzhou Ma and Sebastian Günther

- Commensurate and incommensurate double moire interference in graphene encapsulated by hexagonal boron nitride
  N Leconte and J Jung

2D Materials

Correlated states in super-moiré materials with a kernel polynomial quantics tensor cross interpolation algorithm

Adolfo O Fumega[1] , Marcel Niedermeier[1] and Jose L Lado[*]

Department of Applied Physics, Aalto University, 02150 Espoo, Finland
[1] These authors contributed equally.
[*] Author to whom any correspondence should be addressed.

E-mail: jose.lado@aalto.fi

Abstract

Super-moiré materials represent a novel playground to engineer states of matter beyond the possibilities of conventional moiré materials. However, from the computational point of view, understanding correlated matter in these systems requires solving models with several millions of atoms, a formidable task for state-of-the-art methods. Conventional wavefunction methods for correlated matter scale with a cubic power with the number of sites, a major challenge for super-moiré materials. Here, we introduce a methodology capable of solving correlated states in super-moiré materials by combining a kernel polynomial method with a quantics tensor cross interpolation matrix product state algorithm. This strategy leverages a mapping of the super-moiré structure to a many-body Hilbert space, that is efficiently sampled with tensor cross interpolation with matrix product states, where individual evaluations are performed with a Chebyshev kernel polynomial algorithm. We demonstrate this approach with interacting super-moiré systems with up to several millions of atoms, showing its ability to capture correlated states in moiré-of-moiré systems and domain walls between different moiré systems. Our manuscript puts forward a widely applicable methodology to study correlated matter in ultra-long length scales, enabling rationalizing correlated super-moiré phenomena.

1. Introduction

Twisted moiré materials [1] provide a unique playground to engineer artificial states of matter, including topological states [2–6], correlated phases [7–12], and superconductivity [13–17]. Moiré patterns arise due to the lattice mismatch between two or more van der Waals layers, leading to several coexisting length scales. This can naturally occur when two layers of different van der Waals materials with distinct lattice parameters are stacked together, or when layers of the same material are twisted or strained. Interestingly, when three or more different layers are stacked, the moiré pattern itself can feature a long-range modulation, giving rise to a super-moiré pattern [18–21]. Among super-moiré patterns, for generic twist angles quasiperiodic patterns emerge, where recent experiments have demonstrated even more exotic states [22–24], including competing correlated mosaic orders and quasiperiodic correlated phases, as well as superconductivity [24]. From a

theoretical point of view, understanding the electronic structure of moiré patterns microscopically at the atomistic level requires treating interacting systems with tens of thousands of atoms [25–34], a task that pushes the limits of conventional methods [35]. Modeling super-moiré patterns requires solving systems with millions of atoms and incorporating electronic interactions in a selfconsistent manner, a task challenging beyond current atomistic electronic structure methods.

The problem of dealing with very high-dimensional objects is well-known in physics, in particular in the case of quantum many-body calculations [36–38]. For a quantum many-body system with L sites, the Hilbert space has a dimension of 2^L, making quantum many-body calculations extremely challenging even for moderate system sizes [39, 40]. A very successful strategy to deal with this problem is to use variational tensor network states to parametrize quantum many-body wavefunctions [36, 41–47]. This approach allows us to solve with

nearly arbitrary precision one-dimensional models, and it has provided the most accurate solutions for paradigmatic two-dimensional models such as the doped Hubbard and frustrated Heisenberg models [48–50]. In recent years, it has been realized that the power of tensor networks parametrizing very high-dimensional objects can be applied beyond the realm of quantum many-body physics. This has lead to applications in tensor networks for machine learning [51–56], quantum computing [57–64], and parsimonious function representation [65–68]. In particular, tensor networks can be used to efficiently compress and numerically represent functions that exhibit internal structures. This suggests that this methodology may enable addressing super-moiré systems, whose spatially dependent electronic structure gives rise to phenomena occurring at different length scales.

Here, we demonstrate a technique capable of solving interacting super-moiré structures with several millions of atoms. Our method combines a kernel polynomial method with a quantics tensor cross interpolation (KPQTC) with matrix product states. The methodology maps the super-moiré structure to a many-body Hilbert space, whose mean-field Hamiltonian is compressed in a matrix product state. This tensor network representation of the mean-field Hamiltonian is learned by applying a tensor cross-interpolation algorithm, which greatly reduces the number of real-space correlators which have to be evaluated with the (expensive) kernel polynomial method (KPM). With this methodology, we show that interacting electronic models in real space for systems with millions of atoms can be solved, allowing us to compute interaction-induced symmetry-broken states in those systems while treating interactions in a self-consistent manner. In particular, we show that this technique allows us to efficiently solve interacting super-moiré models in one and two dimensions, and even in the presence of super-moiré domain boundaries. Our results establish a methodology capable of dealing with interacting problems well beyond conventional wavefunction methods, providing a technique capable of addressing correlated physics in super-moiré systems from microscopic models.

The paper is organized as follows. We first introduce and describe the KPQTC methodology that we have developed in this work. In the next two sections, we apply the KPQTC to the study of super-moiré 1D models and 2D materials. Finally, we provide the discussion and conclusion sections highlighting the results and the broad applicability of the KPQTC method.

2. Methods

In the following, we elaborate on the methodology to solve interacting super-moiré systems. We will focus on interacting fermionic models solved at the mean-field level, where the individual mean-field parameters can be computed with a kernel polynomial algorithm. The tensor cross interpolation algorithm allows us to reconstruct the whole mean-field Hamiltonian by iteratively selecting the mean field parameters to be computed.

2.1. Interactions in super-moiré

The Hamiltonian of a super-moiré system in the presence of electronic interactions takes the form

$$H = \sum_{ijs} t_{ij} c^{\dagger}_{i,s} c_{j,s} + \sum_{ijss'} V_{ij} c^{\dagger}_{i,s} c_{i,s} c^{\dagger}_{j,s'} c_{j,s'} \quad (1)$$

where t_{ij} are the hopping parameters in the system and V_{ij} parametrizes the electronic interactions. To find the ground state of the Hamiltonian above, the interacting term can be decoupled with a mean-field ansatz of the form $V_{ij} c^{\dagger}_{i,s} c_{i,s} c^{\dagger}_{j,s'} c_{j,s'} \approx V_{ij} \langle c^{\dagger}_{i,s} c_{i,s} \rangle c^{\dagger}_{j,s'} c_{j,s'} + \dots$ where ... is a shorthand for the remaining Wick contractions. The previous decoupling gives rise to a mean-field Hamiltonian of the form

$$H_{\mathrm{MF}} = \sum_{ijs} t_{ij} c^{\dagger}_{i,s} c_{j,s} + \sum_{ijss'} \chi_{ijss'} c^{\dagger}_{i,s} c_{j,s'} \quad (2)$$

with $\chi_{ijss'} \equiv \chi_{ijss'}(V_{ij}, |\mathrm{GS}\rangle)$ the mean-field parameters, where $|\mathrm{GS}\rangle$ is the variational many-body ground state $H_{\mathrm{MF}}|\mathrm{GS}\rangle = E_{\mathrm{GS}}|\mathrm{GS}\rangle$. The variational ground state is taken as a product state of the form $|\mathrm{GS}\rangle = \prod_{\alpha} \psi^{\dagger}_{\alpha}|\Omega\rangle$, with $\psi^{\dagger}_{\alpha}$ variational single-particle states and $|\Omega\rangle$ the vacuum state, $\psi_{\alpha}|\Omega\rangle = 0$. As H_{MF} depends on the $|\mathrm{GS}\rangle$, and $|\mathrm{GS}\rangle$ depends on H_{MF}, the previous problem can be solved with a conventional iterative self-consistent algorithm. From the computational point of view, the most demanding step consists of computing the mean-field parameters $\chi_{ijss'}$ at each step of the self-consistent procedure. In particular, for a super-moiré system with N sites, conventional algorithms based on matrix diagonalization as implemented in electronic structure codes scale as N^3, whereas a full Chebyshev expansion reduces the computational cost to N^2. This sets the maximum number of sites computable with typical computational resources with diagonalization on the order of $N = 10^4$ atoms, and with Chebyshev expansion in $N = 10^6$ atoms. Modeling interacting states in super-moiré materials requires solving problems with several millions of atoms, well above the capabilities of the previous two methods.

2.2. Interactions with a kernel polynomial expansion

We now address how a Chebyshev kernel polynomial expansion can be used to solve self-consistent mean-field systems. In each iteration of the self-consistent
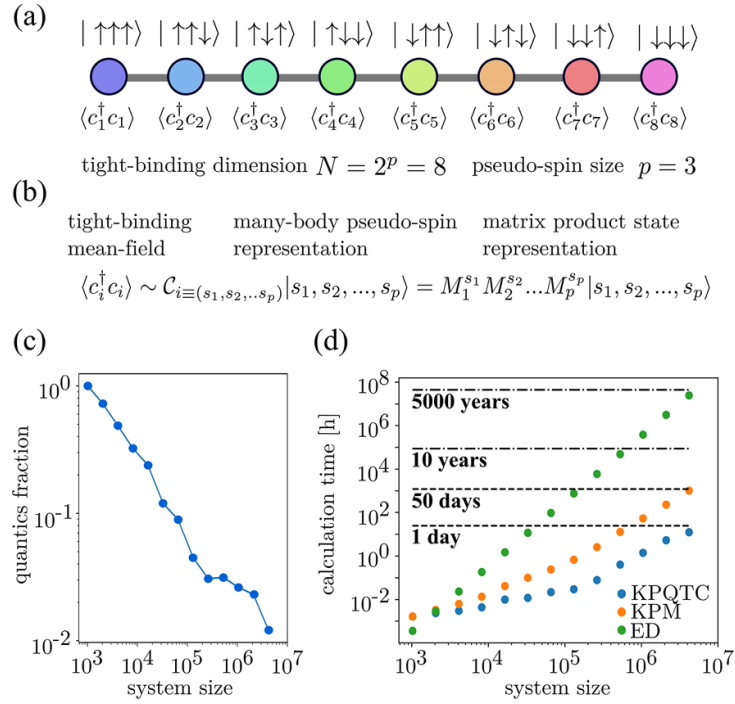
Figure 1. (a) Schematic of the mapping between an interacting super-moiré and an auxiliary many-body spin model. A many-body pseudo spin model with p spins allows us to encode the mean-field of a tight binding model with 2^p sites. (b) The interacting mean-field is encoded as the amplitude of a many-body spin model as a matrix product state. Panel (c) shows the compression of the mean-field for different system sizes achieved by the algorithm. Panel (d) shows a comparison between our algorithm (KPQTC), a pure KPM method and exact diagonalization (ED).

procedure, the variational parameters of the mean-field Hamiltonian $\chi_{ijss'}$ can be calculated once the correlators $\langle c^\dagger_{i,s} c_{j,s'} \rangle \equiv \langle \mathrm{GS} | c^\dagger_{i,s} c_{j,s'} | \mathrm{GS} \rangle$ are known. These correlators can be computed as

$$\langle c^\dagger_{i,s} c_{j,s'} \rangle = \int_{-\infty}^{\epsilon_F} \langle \Omega | c_{j,s'} \delta\left(\omega - \mathcal{H}_{\mathrm{MF}}\right) c^\dagger_{i,s} | \Omega \rangle \, d\omega \quad (3)$$

where ϵ_F is the single particle Fermi energy and $\delta(\omega - \mathcal{H}_{\mathrm{MF}})$ is the Dirac-delta function operator. Taking $\langle c^\dagger_{i,s} c_{j,s'} \rangle = \int_{-\infty}^{\epsilon_F} g_{ijss'}(\omega) d\omega$, with $g_{ijss'}(\omega) = \langle \Omega | c_{j,s'} \delta(\omega - \mathcal{H}_{\mathrm{MF}}) c^\dagger_{i,s} | \Omega \rangle$, where $g_{ijss'}(\omega)$ is the dynamical correlator between sites i and j with spin s and s', and $|\Omega\rangle$ is the empty many-body state. For the sake of concreteness, we now take that the Hamiltonian $\mathcal{H}_{\mathrm{MF}}$ has a single particle spectrum bounded in the interval $(-1, 1)$. The function $g_{ijss'}(\omega)$ can be efficiently computed with a Chebyshev kernel polynomial expansion [69] of the form $g_{ijss'}(\omega) = \frac{1}{\pi\sqrt{1-\omega^2}}[\gamma_0 T_0(\omega) + 2\sum_{n>0} \gamma_n T_n(\omega)]$, where $T_n(\omega)$ are the Chebyshev polynomials and γ_n are the coefficients of the expansion. Thanks to the Chebyshev recursion relation, the moments of the expansion can be computed as $\gamma_n = \langle \Omega | c_{j,s'} | v_n \rangle$, where $|v_{n+1}\rangle = 2\mathcal{H}_{\mathrm{MF}} |v_n\rangle - |v_{n-1}\rangle$, with $|v_1\rangle = \mathcal{H}_{\mathrm{MF}} |v_0\rangle$ and $|v_0\rangle = c^\dagger_{i,s} |\Omega\rangle$. The calculation of a single correlator $\langle c^\dagger_{i,s} c_{j,s'} \rangle$ scales linearly with the number of atoms N. To compute the self-consistent Hamiltonian, the number of correlators that have to be evaluated is proportional to the number of atoms N, so that a

Chebyshev kernel polynomial expansion allows us to perform self-consistent calculations [70] with a scaling N^2, in contrast the scaling N^3 for ED.

2.3. Quantics tensor-network representation of the mean-field Hamiltonian

The most expensive part of the algorithm is to evaluate the variational parameters $\chi_{ijss'}$ of the mean-field Hamiltonian. The $\chi_{ijss'}$'s depend on the correlators $\langle c^\dagger_{i,s} c_{j,s'} \rangle = \langle \mathrm{GS} | c^\dagger_{i,s} c_{j,s'} | \mathrm{GS} \rangle$, and where each $\langle c^\dagger_{i,s} c_{j,s'} \rangle$ has to be found by performing a full run of the KPM algorithm. Therefore, to perform the full mean-field calculation, a large number of KPM's has to be executed. In the following, we will apply the tensor cross interpolation algorithm to construct an approximation of the function $\chi_{ijss'}(\{\langle c^\dagger_{i,s} c_{j,s'} \rangle\})$ as a matrix product state:

$$\chi_{ijss'} \approx M_1^{s_1} M_2^{s_2} \dots M_p^{s_p}. \quad (4)$$

The main benefit of this method is, that it allows us to construct a high-fidelity approximation of $\chi_{ijss'}$, while only requiring an exact evaluation for a very small number of arguments $\langle c^\dagger_{i,s} c_{j,s'} \rangle$. All other correlators, that are not called during the construction of $\chi_{ijss'}$, do not need to be calculated in the first place, which greatly reduces the number of individual KPM runs, the most expensive part of the algorithm. A schematic of the mapping used by the KPQTC is shown in figure 1.

The kernel polynomial tensor cross interpolation method relies on exploiting the natural structure and length scales of the mean-field Hamiltonian in a super-moiré system. The large number of components of $\chi_{ijss'}(\{\langle c_{i,s}^\dagger c_{j,s'} \rangle\})$ can be reformulated as a rank-R tensor $\chi^{\sigma_1 \cdots \sigma_R}$, with $R \propto \log(\text{number of correlators})$. This tensor can be re-expressed as a much cheaper matrix product state, using the tensor cross interpolation algorithm, which learns a quasi-optimal approximation of $\chi^{\sigma_1 \cdots \sigma_R}$ by evaluating it exactly for only a small subset of its entries [65, 71–76]. Therefore, only a small subset of the full list $[\langle c_1^\dagger c_1 \rangle, \ldots, \langle c_{2^p}^\dagger c_{2^p} \rangle]$ of real-space correlators has to be calculated in practice. Furthermore, the architecture of the underlying matrix product state and the update strategy is dynamically optimized during the self-consistent loop, where at each iteration we optimize for the strategy that requires the least amount of evaluations of the mean-field of the previous iteration. The dynamically optimized parameters include the matrix product state bond dimension, the number of orbitals for which independent matrix product states are created, the initial pivot, the choice of a rook or accumulative optimization method, and the number and location of global pivots. The convergence of the MPS representation of the mean-field Hamiltonian is controlled by two main parameters: the maximum bond dimension and a per-tensor singular value decomposition-compression error. Our methodology sets a value of the compression error and lets the algorithm make evaluations until the matrix product state constructed has enough accuracy. This is thus an iterative procedure that is only halted when the mean-field is accurate enough. The threshold we set in the matrix product state construction is taken as one order of magnitude below the target error of the selfconsistency loop, guaranteeing that the mean-field features high enough accuracy.

3. Interactions in super-moiré 1D models

We now use the KPQTC method to address one-dimensional models. First, we will focus on a system that features two incommensurate moiré patterns, also incommensurate with the lattice. Second, we will address a system featuring an interface between two moiré patterns, to show that the methodology is able to deal with inhomogeneous problems. While 1D models are not the most relevant use case for van der Waals materials, they provide an excellent testing ground for the KPQTC algorithm to show that calculations with millions of atoms can be performed.

3.1. Incommensurate 1D super-moiré
We first consider a model featuring two moiré patterns, incommensurate with each other and with

the original lattice. Super-moiré models can be realized in artificial platforms including engineering optical resonators and cold atom systems [77, 78]. Furthermore, within van der Waals materials, the electronic properties of multi-walled nanotubes are effectively described by a one-dimensional super-moiré Hamiltonian [79]. We take a Hamiltonian of the form

$$\mathcal{H} = \sum_{ij,s} t_{ij} c_{i,s}^\dagger c_{j,s} + U \sum_i \left[c_{i,\uparrow}^\dagger c_{i,\uparrow} - \frac{1}{2} \right] \left[c_{i,\downarrow}^\dagger c_{i,\downarrow} - \frac{1}{2} \right],$$
(5)

where the hopping is modulated by two incommensurate moiré patterns as

$$t_{n,n+1} = t_0 + t_1 \cos(k_1 X_{n,n+1}) + t_2 \cos(k_2 X_{n,n+1}),$$
(6)

with $X_{n,n+1} = (x_n + x_{n+1})/2$, k_1 and k_2 the wavevectors of the two moirés and x_n is the location of site n. We take $k_1 = 2\pi/5\sqrt{2}$ and $k_2 = 2\pi 5/2^{p-1}\sqrt{3}$, which leads to two incommensurate modulations, also incommensurate with the lattice. The modulation in the local hopping gives rise to a different competition between electronic interactions and kinetic energy in different regions in the system. We solve the model with the QTCI for a system with $L = 2^{22}$ sites, approximately 4 million atoms. The results of our calculation are shown in figure 2, where we show the moiré modulation of the Hamiltonian at the two length scales, together with the non-interacting (figure 2(b)) and interacting (figure 2(c)) local spectral function. In particular, we observe that interactions give rise to a spatially dependent gap opening, as shown by comparing the density of states in the absence (figure 2(b)) and presence (figure 2(c)) of electronic interactions. Interestingly, on the largest length scale, the gap opening fully follows the moiré length scale, whereas, on the shorter length scale, the spectrum shows a modulation of the spectral weight. This stems from the fact that at the smaller moiré length scale, the correlation length associated with the electronic order is of the same order as the moiré length scale, which gives rise to the lowest electronic excitation to extend in the whole moiré. In contrast, for the biggest moiré length scale, the correlation length associated with the order is much smaller than the length scale of the moiré, which leads to the spectral gap being modulated exactly following the moiré.

The performance of the KPQTC method [80, 81] as compared to the current techniques is highlighted in figure 1. Figure 1(c) shows the compression of the mean-field components achieved by the KPQTC. The fraction of real-space correlators required as compared to the pure KPM is plotted as a function of the system size. We can clearly observe the advantage
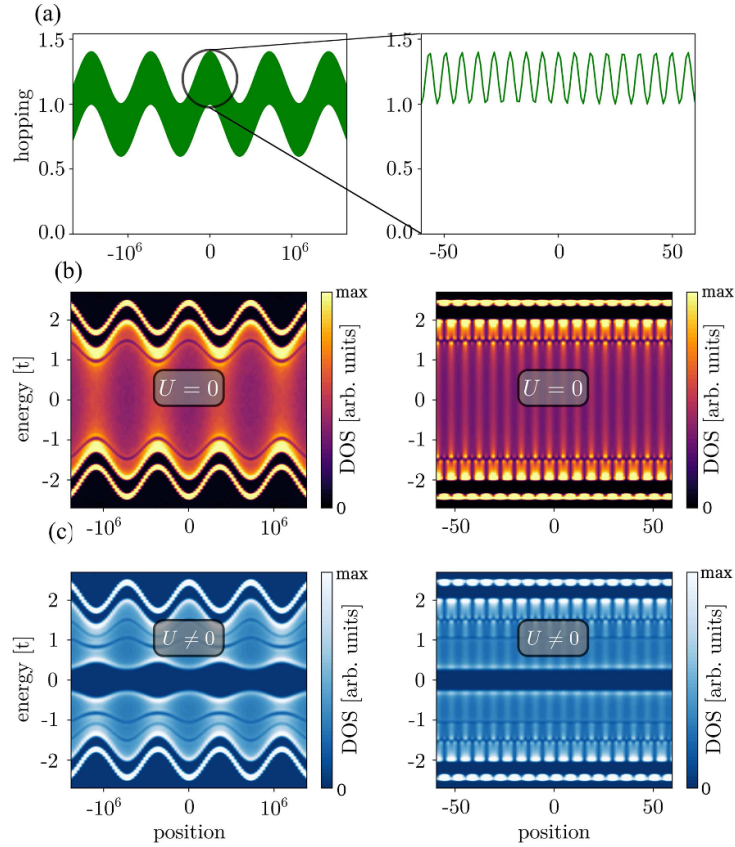
Figure 2. Correlated super-moiré for $L = 2^{22}$ sites (above 4 million sites). Panel (a) shows the super-moiré modulation of the Hamiltonian, featuring a moiré pattern at short scales, and another at long length scales. Panel (b) shows the density of states in the system at long and short length scales, showing how its spectral properties are modulated. Panel (c) shows the spectral function of the interacting super-lattice solved selfconsistently with KPQTC. It is observed that the interaction-induced gap in the spectral function is modulated in the long length scale, whereas its intensity is modulated at the short length scale.

introduced by the KPQTC method for large systems above 10^5 sites, where the fraction of correlators required decreases as the system size grows. The convergence time of the self-consistent mean-field calculation for the KPQTC method is reported in figure 1(d). We show the estimated calculation times for the pure KPM and the ED methods are shown for comparison. We can observe that our KPQTC allows solving systems of millions of atoms in less than one day, while the traditional KPM requires around 50 days. KPM and KPQTC become faster than exact diagonalization once the system size goes above 10^3. sites, and KPQTC becomes substantially faster than KPM for systems above 10^5 sites. Therefore, these results demonstrate the advantage of the KPQTC method to study correlated states in super-moiré materials composed of millions of atoms.

3.2. Super-moiré domain wall in 1D
An alternative situation that appears in super-moiré systems is a domain wall between different length scales. This emerges in situations where structural relaxations strongly prefer specific stacking or moiré length scales, a phenomenon that gives rise to domain walls appearing between different regions. We will here consider a system where the shortest moiré

length scale is the same in the whole system, whereas the biggest one features two domains. We take the hopping $t_{n,n+1}$ to be modulated in space by two wavelengths k_1 and $\bar{k}_2$, one of them spatially dependent

$$t_{n,n+1} = t_0 + t_1 \cos(k_1 X_{n,n+1}) + t_2 \cos(\bar{k}_2 (X_{n,n+1}) X_{n,n+1}), \quad (7)$$

with the wavelength of the modulation featuring a domain wall:

$$\bar{k}_2 (X_{n,n+1}) = \bar{k}_2 (1 + \delta \tanh(X_{n,n+1}/W)). \quad (8)$$

Here, W describes the width of the domain wall and δ parametrizes the mismatch between the length scales of the moiré modulations in the two domains, that in the asymptotic limit are $k_2(1-\delta)$ and $k_2(1+\delta)$. In our calculations, we have used $\delta = 0.2$, $W = 2^p/40$, $k_2 = 2\pi 5/2^{p-1}\sqrt{3}$ and $k_1 = 2\pi/5\sqrt{2}$. This Hamiltonian therefore describes a system breaking translational symmetry regardless of the moiré length. In figure 3, we show the solution of the interacting model for 2^{21} sites, or approximately 2 million atoms. The impact of the electronic interactions can be observed by comparing the non-interacting (figure 3(b)) and interacting (figure 3(c)) spectral
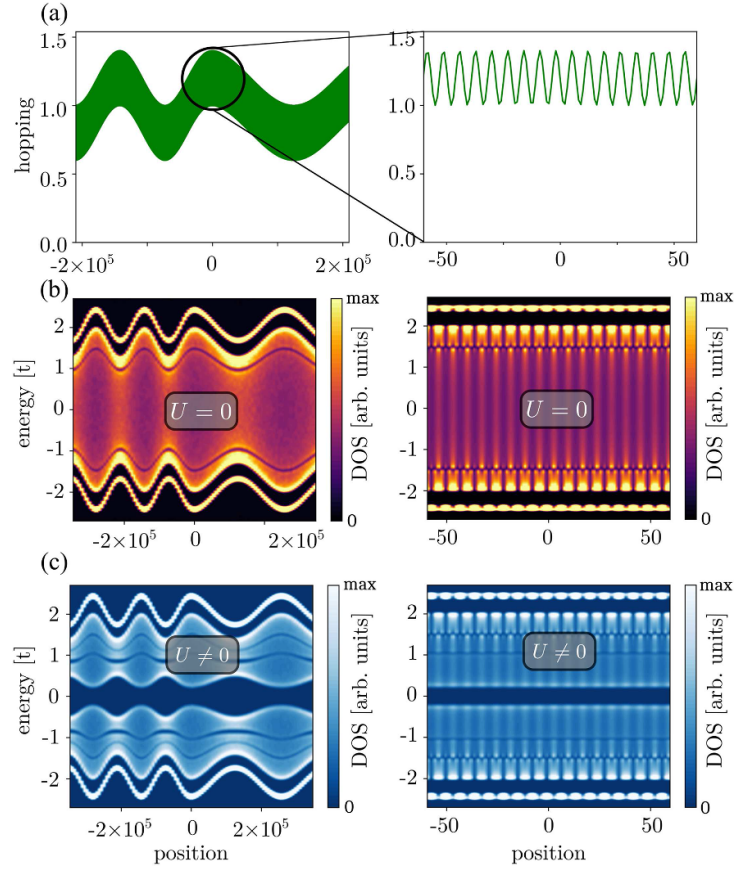
Figure 3. Correlated super-moiré domain wall for $L = 2^{20}$ sites (above 1 million sites). Panel (a) shows the super-moiré modulation featuring a domain wall, featuring different super-moiré modulations at the left and right boundary. Panel (b) shows the density of states in the system at long and short length scales, showing how its spectral properties are modulated according to each domain. Panel (c) shows the spectral function of the interacting system solved selfconsistently with KPQTC. The interaction-induced gap in the spectral function is modulated in the long length scale following the super-moiré at each domain, whereas at the domain wall its intensity is modulated following the local moiré.

functions. The gap in the spectral function follows the moiré pattern both in the left and right domains at the longest length scale. As in the case studied previously, this phenomenology stems from the fact that both moiré length scales are much longer than the localization length associated with the correlated state, which leads to a spectral gap reflecting the large-scale moiré modulation. At shorter scales, the spectrum is modulated according to the moiré, but leading to a spectral gap that is uniform due to the comparable correlation and moiré length scales.

4. Interactions in super-moiré 2D materials

We now consider interacting super-moiré materials in two dimensions, which is the most physically relevant scenario for van der Waals materials. We will focus on the Hamiltonian of a purely two-dimensional system of super-moiré graphene monolayer. moiré patterns in monolayer graphene can emerge from periodically modulated strain from buckling [82–86], or from a moiré pattern with boron nitride. For the sake of concreteness, we will focus on the case of periodically buckled monolayer graphene, which has been
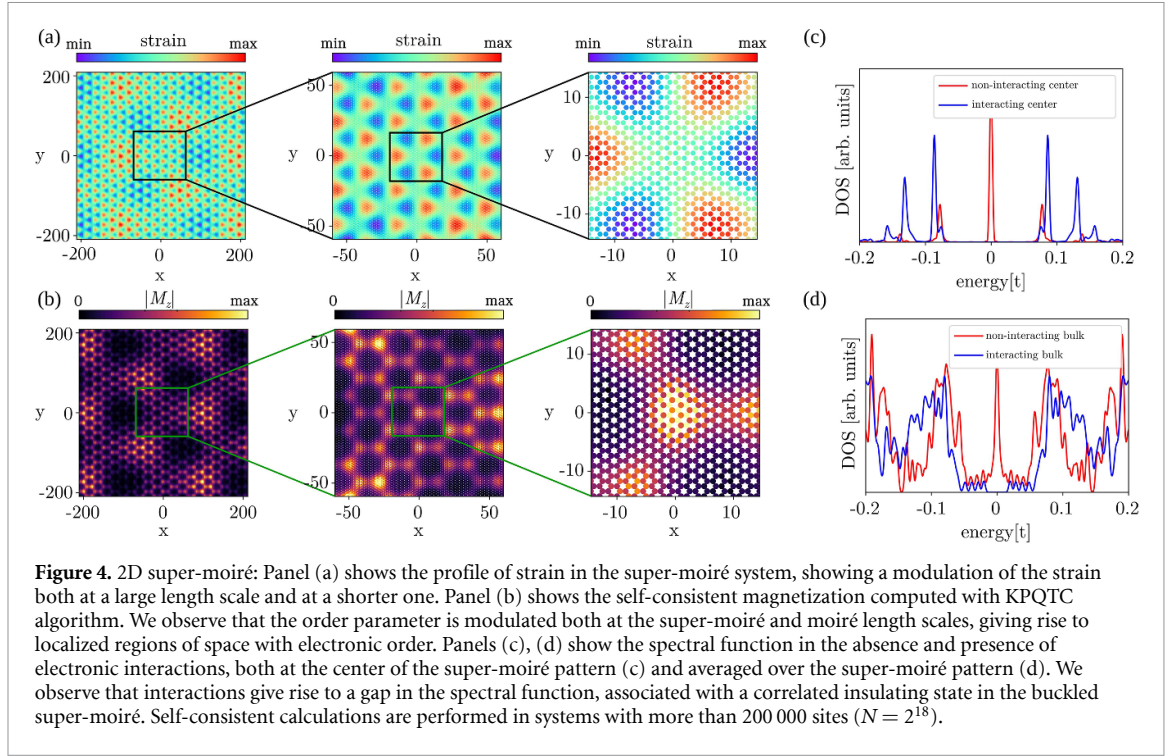
demonstrated to lead to a variety of correlated states. The Hamiltonian of the system thus takes the form

$$\mathcal{H} = \sum_{\langle ij \rangle, s} t_{ij} c_{i,s}^\dagger c_{j,s} + U \sum_i \left[c_{i,\uparrow}^\dagger c_{i,\uparrow} - \frac{1}{2} \right] \left[c_{i,\downarrow}^\dagger c_{i,\downarrow} - \frac{1}{2} \right],$$

(9)

where the sites ij form a honeycomb lattice and $\langle ij \rangle$ runs over the first neighbors in the graphene honeycomb lattice. In the presence of buckling, the hopping parameters t_{ij} of graphene are modified as [83, 85, 86]

$$t_{ij} = t_{ij}^0 \left(1 + \delta \sin \left(\Omega \mathbf{u}_{ij} \cdot \mathbf{R}_{ij} \right) \right),$$

(10)

where $\mathbf{R}_{ij} = (\mathbf{r}_i + \mathbf{r}_j)/2$ is the location of the bond, u_{ij} is the vector linking sites i and j, and Ω parametrizes the frequency of the buckling. The previous modulation gives rise to a direction-dependent modulation of the hopping of wavevector Ω. The previous buckling modulation gives rise to pseudo-Landau levels due to the emergence of a non-uniform artificial gauge field. The pseudo-Landau levels get localized in an emergent honeycomb lattice structure due to the modulation of the gauge field. In the presence

Figure 4. 2D super-moiré: Panel (a) shows the profile of strain in the super-moiré system, showing a modulation of the strain both at a large length scale and at a shorter one. Panel (b) shows the self-consistent magnetization computed with KPQTC algorithm. We observe that the order parameter is modulated both at the super-moiré and moiré length scales, giving rise to localized regions of space with electronic order. Panels (c), (d) show the spectral function in the absence and presence of electronic interactions, both at the center of the super-moiré pattern (c) and averaged over the super-moiré pattern (d). We observe that interactions give rise to a gap in the spectral function, associated with a correlated insulating state in the buckled super-moiré. Self-consistent calculations are performed in systems with more than 200 000 sites ($N = 2^{18}$).

of interactions, those localized modes give rise to a correlated state.

We will study two cases where super-moiré physics emerges in this system. First, we will consider the case where two different bucklings at different length scales emerge, with relative frequencies Ω_M and Ω_{SM} and strengths δ_M and δ_{SM}. Afterwards, we will consider an interface between two buckling modulations.

4.1. Correlations in a 2D super-moiré

We start first with the moiré of moiré buckling. In this scenario, the hoppings of the graphene monolayer are modulated as
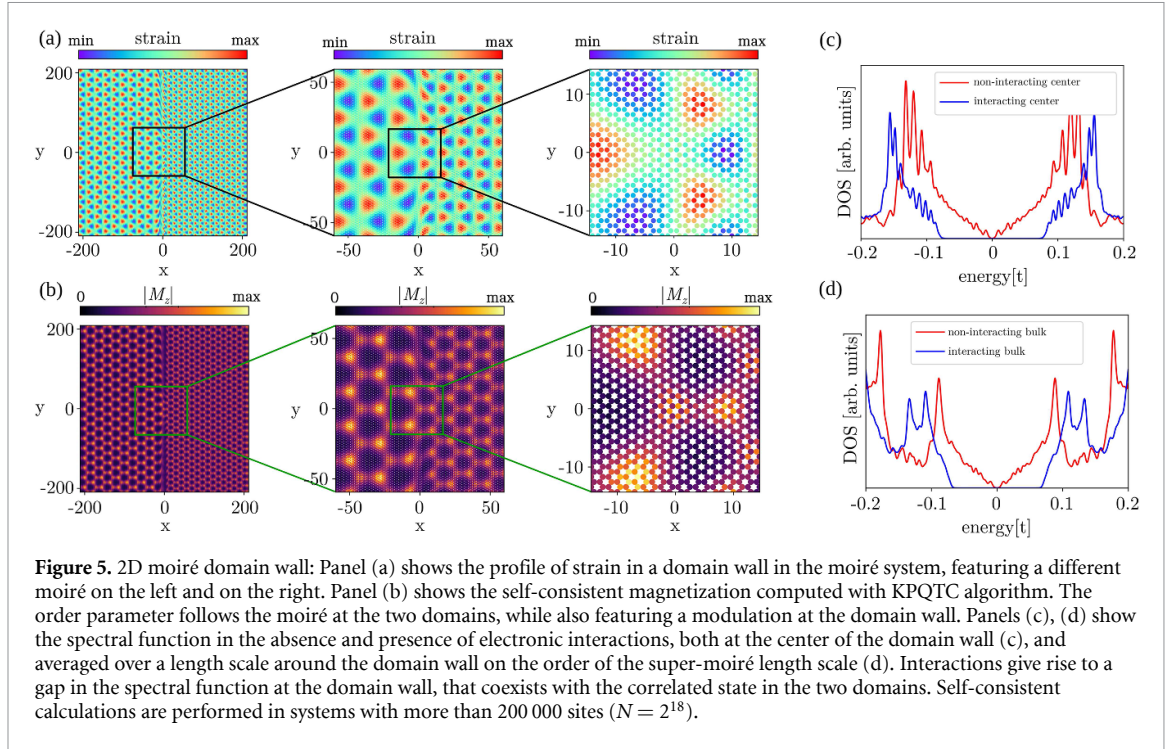
$$
\begin{aligned}
t_{ij} = t_{ij}^0 &\left(1 + \delta_M \sin \left(\Omega_M \mathbf{u}_{ij} \cdot \mathbf{R}_{ij} \right) \right) \\
&\times \left(1 + \delta_{SM} \sin \left(\Omega_{SM} \mathbf{u}_{ij} \cdot \mathbf{R}_{ij} \right) \right), \quad (11)
\end{aligned}
$$

where δ_M and δ_{SM} correspond to the strength of the buckling at the moiré and super-moiré length scales, and Ω_M, Ω_{SM} are the wavevectors of the moiré and super-moiré buckling. We take $\Omega_M = 2\pi\sqrt{2}/30$, $\Omega_{SM} = \Omega_M/7$, $U = 2t$, $\delta_M = 0.2$ and $\delta_{SM} = 0.1$. In figure 4(a), we show the strength of the local strain field at each point in space, defined as the average value of the neighboring hopping $s(\mathbf{r}_i) \sim \sum_j t_{ij}$. We solve a system with 2^{18}, or approximately 200 000, sites, where the self-consistent magnetization is shown in figure 4(b). We observe that the symmetry broken order clearly follows both moiré patterns, giving rise to an emergent honeycomb lattice modulated at the super-moiré length scale of magnetic order. We can now compare the spectral

function of the system both with and without interactions, as shown in figures 4(c) and (d). In particular, in figure 4(c) we show the local spectral function right at the center of the super-moiré pattern. In the absence of interactions, a zero energy peak emerges, which in the presence of interactions gives rise to a gap (figure 4(c)). Such zero energy mode is precisely the one responsible for the spatially localized magnetic order as shown in the shortest length scale of figure 4(b). Figure 4(d) shows the comparison of the spectral function computed in the whole length scale of the super-moiré pattern. We observe that in the absence of correlations, the system features a gapless electron gas with a van Hove singularity at charge neutrality, whereas in the presence of interactions a full band gap opens up (figure 4(d)). Such a van Hove singularity corresponds to the localized modes in specific regions of the moiré pattern, which in the interacting regime give rise to a correlated insulator in the full system.

4.2. Correlations between moiré domains

In the presence of two moiré patterns stemming from several twisted two-dimensional materials, structural relaxations can lead to relatively uniform moiré regions separated from each other by domain walls [21, 87–89]. This phenomenology observed experimentally requires that computational methods be capable of dealing with geometries lacking translational symmetry and hosting a very large amount of atoms. We now show that the KPQTC methodology is able to capture correlated states emerging in the presence of moiré domains. For the sake of concreteness,

Figure 5. 2D moiré domain wall: Panel (a) shows the profile of strain in a domain wall in the moiré system, featuring a different moiré on the left and on the right. Panel (b) shows the self-consistent magnetization computed with KPQTC algorithm. The order parameter follows the moiré at the two domains, while also featuring a modulation at the domain wall. Panels (c), (d) show the spectral function in the absence and presence of electronic interactions, both at the center of the domain wall (c), and averaged over a length scale around the domain wall on the order of the super-moiré length scale (d). Interactions give rise to a gap in the spectral function at the domain wall, that coexists with the correlated state in the two domains. Self-consistent calculations are performed in systems with more than 200 000 sites ($N = 2^{18}$).

we will focus on studying a domain wall between two different bucklings in graphene. In this scenario, the hopping of the graphene system will be modulated as

$$t_{ij} = t_{ij}^0 \left(1 + \delta \sin \left(\Omega \left(\mathbf{R}_{ij} \right) \mathbf{u}_{ij} \cdot \mathbf{R}_{ij} \right) \right), \qquad (12)$$

where now the buckling wavevector changes in space and features a domain wall of the form

$$\Omega \left(\mathbf{R}_{ij} \right) = \Omega_0 \left(1 + \gamma \tanh \left(X_{ij}/W \right) \right). \qquad (13)$$

Here W parametrizes the width of the moiré domain wall and γ controls the difference between the two moiré buckling frequencies, which asymptotically inside the domain become $\Omega_0(1 - \gamma)$ and $\Omega_0(1 + \gamma)$. We take $\Omega_0 = 2\pi\sqrt{2}/23$, $\gamma = 0.3$, $U = 2t$, and $\delta = 0.2$.

The spatial modulation of the strain is shown in figure 5(a) at different length scales. At the right and left domains the strain profile corresponds to a buckled monolayer, yet featuring different modulation length scales. When introducing electronic interactions (figure 5(b)), a moiré correlated state emerges, featuring an order parameter following the modulation of the strain in the left and right domains. Interestingly, certain regions develop a correlated order at the interface between the two domains, whereas in other regions of the domain wall, the correlated order is quenched (figure 5(b)). This phenomenology is due to the mismatch in the non-uniform strain between the two domains in different regions of the domain wall. With the correlated state, the spectral function of the system can be computed both at the center of the domain wall (figure 5(c)), or averaged over a large length scale (figure 5(d)). In

the absence of interactions, the system remains gapless, featuring a linear dispersion close to the domain wall (figure 5(c)). In the presence of interactions, the whole system develops a correlated insulating state, including the domain wall, thus giving rise to a full spectral gap in the system (figure 5(d)).

5. Discussion

We have shown that the kernel polynomial tensor cross algorithm enables us to solve interacting super-moiré models with several millions of atoms. While our calculations focus on Hubbard models, our methodology can be used to compress and infer a generic mean-field Hamiltonian, including in the presence of non-local interactions. In particular, beyond the magnetic orders we have considered in our manuscript, it is worth noting that a similar strategy can be used to capture charge order, superconducting or valley coherent states [10], which are especially relevant for twisted graphene multilayers. The energy resolution of our algorithm is set by the number of Chebyshev polynomials. Symmetry-broken states with very small energy scales, such as superconducting order, require a higher number of Chebyshev polynomials. A key step is that the models we considered have a certain structure, both in the single-particle Hamiltonian and its mean-field. The tensor cross interpolation algorithm relies on the existence of a compressibility in the mean-field Hamiltonian.

While this is true for generic twisted van der Waals materials, even in the presence of domain walls, systems with strong disorder may represent a challenge

for our algorithm. This stems from the fact that in the presence of strong disorder, the compressibility of the mean-field is lost due to randomness, thus substantially increasing the required number of evaluations to reconstruct the mean-field. This is however not a limitation in the presence of a finite dilute amount of impurities, and thus the KPQTC methodology would allow us to tackle super-moiré systems with a small amount of impurities. It is important to note that the choice of pivots and update strategy of tensors can strongly influence the required number of evaluations required to converge the tensor network. As work in quantics tensor cross interpolation methods is progressing rapidly, we foresee that further improvements in these algorithms will enable us to address more complex and bigger interacting super-moiré systems.

In our manuscript, we have used a matrix product state representation of the mean-field terms, yet the Hamiltonian is still stored as a sparse matrix. With this algorithm, the maximum system size is determined by the required kernel polynomial expansion with vector for N sites, which requires storing vectors of size N, where memory becomes the bottleneck. A potential step in the future is to store the Hamiltonian itself as a matrix product operator, such that the kernel polynomial expansion is done directly with tensor networks. This would allow us to reach system sizes beyond $N = 10^8$. It is also worth noting that since the evaluations of each individual correlator with the kernel polynomial algorithm are fully independent, our approach can be massively parallelized to thousands of cores almost with linear scaling [90]. This should be contrasted with electronic structure methods based on diagonalization, where diagonalization tasks show a worse than linear scaling with parallelization. While our calculations have focused on correlated states in tight binding models, a similar approach to the one presented here can be implemented in conventional Hartree–Fock quantum chemistry codes and density functional theory, in particular, those based on describing the electronic density and Hamiltonian on real space grids [91–95].

While our demonstration above focuses on a super-moiré pattern in a graphene monolayer, our methodology can be readily extended to twisted multilayers. Experiments in moiré systems are rapidly developing [96, 97], with notable demonstrations including super-moiré twisted multilayer graphene and other van der Waals heterostructures [18–21]. In particular, twisted graphene trilayers provide an exceptional platform to observe the effects of super-moiré patterns in the case where different twisting angles are taken between the top and bottom layers [24]. Spectroscopic measurements with scanning tunneling microscopy have been performed in a variety of correlated twisted graphene heterostructures [16, 98–100], and it is expected

that future experiments will enable probing the unique physics of super-moiré patterns in real-space. Scanning probe experiments are particularly promising for directly validating symmetry broken states, as a comparison of the local reconstruction of the spectral function in different regions of the super-moiré provides a highly non-trivial test for a correlated state [16, 100]. This can be especially interesting to characterize incommensurate Kekule symmetry broken states in twisted graphene multilayers [10]. We expect that our methodology will enable understanding of a variety of symmetry-broken correlated states in super-moiré systems, whose system sizes are well beyond the capabilities of conventional methods. We finally note that our methodology has no fundamental limitation to considering other systems that can be captured with mean-field theory, and it is not limited to van der Waals materials. In particular, our method can be used for generic symmetry-broken states that have very long length scales, such as incommensurate charge density waves in high temperature superconductors [101, 102] or incommensurate charge density waves in transition metal chalcogenides [103–105].

6. Conclusion

Solving interacting models in super-moiré materials represents a formidable theory challenge to understanding emerging phenomena in van der Waals materials, due to the unprecedented system sizes required to capture their physics. Here, we have presented a kernel polynomial tensor cross interpolation algorithm, that can solve interacting models with several millions of atoms, considerably outperforming the current state-of-the-art. Our strategy relies on mapping the mean-field Hamiltonian of a large electronic model to an auxiliary many-body Hilbert space that is compressed using a many-body tensor network. The tensor network is constructed with a tensor cross interpolation algorithm, which greatly reduces the number of individual evaluations performed with a KPM. This demonstrates how a quantum-inspired methodology enables massive speed-up of the calculation of mean-field interacting ground states of tight-binding models. We have applied our algorithm to both one- and two-dimensional models, showing that this approach allows us to deal with interacting problems with multiple long-range modulations and domain walls. In particular, we have demonstrated that this methodology can describe correlated states in super-moiré buckled graphene, capturing both the electronic reconstructions and symmetry-breaking at the moiré and super-moiré length scales. Our methodology enables tackling the interacting models with a number of sites required to rationalize the physics of a whole new family of artificial materials based on

twisted van der Waals heterostructures. In particular, it can be readily extended to account for charge order, bond-ordered, topological and superconducting states, providing the required computational tool to study super-moiré quantum matter.

Data availability statement

All data that support the findings of this study are included within the article (and any supplementary files).

ORCID iDs

Adolfo O Fumega ⬤ https://orcid.org/0000-0002-3385-6409
Jose L Lado ⬤ https://orcid.org/0000-0002-9916-1589

References

[1] Andrei E Y, Efetov D K, Jarillo-Herrero P, MacDonald A H, Mak K F, Senthil T, Tutuc E, Yazdani A and Young A F 2021 The marvels of moiré materials *Nat. Rev. Mater.* **6** 201–6
[2] Zeng Y, Xia Z, Kang K, Zhu J, Knüppel P, Vaswani C, Watanabe K, Taniguchi T, Mak K F and Shan J 2023 Thermodynamic evidence of fractional chern insulator in moiré MoTe$_2$ *Nature* **622** 69–73
[3] Serlin M, Tschirhart C L, Polshyn H, Zhang Y, Zhu J, Watanabe K, Taniguchi T, Balents L and Young A F 2020 Intrinsic quantized anomalous hall effect in a moiré heterostructure *Science* **367** 900–3
[4] Sharpe A L, Fox E J, Barnard A W, Finney J, Watanabe K, Taniguchi T, Kastner M A and Goldhaber-Gordon D 2019 Emergent ferromagnetism near three-quarters filling in twisted bilayer graphene *Science* **365** 605–8
[5] Rickhaus P *et al* 2018 Transport through a network of topological channels in twisted bilayer graphene *Nano Lett.* **18** 6725–30
[6] Cai J *et al* 2023 Signatures of fractional quantum anomalous hall states in twisted MoTe$_2$ *Nature* **622** 63–68
[7] Cao Y *et al* 2018 Correlated insulator behaviour at half-filling in magic-angle graphene superlattices *Nature* **556** 80–84
[8] Burg G W, Khalaf E, Wang Y, Watanabe K, Taniguchi T and Tutuc E 2022 Emergence of correlations in alternating twist quadrilayer graphene *Nat. Mater.* **21** 884–9
[9] Kerelsky A *et al* 2019 Maximized electron interactions at the magic angle in twisted bilayer graphene *Nature* **572** 95–100
[10] Kim H *et al* 2023 Imaging inter-valley coherent order in magic-angle twisted trilayer graphene *Nature* **623** 942–8
[11] Lu X *et al* 2019 Superconductors, orbital magnets and correlated states in magic-angle bilayer graphene *Nature* **574** 653–7
[12] Zhao W, Shen B, Tao Z, Han Z, Kang K, Watanabe K, Taniguchi T, Mak K F and Shan J 2023 Gate-tunable heavy fermions in a moiré kondo lattice *Nature* **616** 61–65
[13] Cao Y, Fatemi V, Fang S, Watanabe K, Taniguchi T, Kaxiras E and Jarillo-Herrero P 2018 Unconventional superconductivity in magic-angle graphene superlattices *Nature* **556** 43–50
[14] Yankowitz M, Chen S, Polshyn H, Zhang Y, Watanabe K, Taniguchi T, Graf D, Young A F and Dean C R 2019 Tuning superconductivity in twisted bilayer graphene *Science* **363** 1059–64
[15] Park J M, Cao Y, Watanabe K, Taniguchi T and Jarillo-Herrero P 2021 Tunable strongly coupled superconductivity in magic-angle twisted trilayer graphene *Nature* **590** 249–55
[16] Oh M, Nuckolls K P, Wong D, Lee R L, Liu X, Watanabe K, Taniguchi T and Yazdani A 2021 Evidence for unconventional superconductivity in twisted bilayer graphene *Nature* **600** 240–5
[17] Park J M, Cao Y, Xia Li-Q, Sun S, Watanabe K, Taniguchi T and Jarillo-Herrero P 2022 Robust superconductivity in magic-angle multilayer graphene family *Nat. Mater.* **21** 877–83
[18] Devakul T, Ledwith P J, Xia Li-Q, Uri A, de la Barrera S C, Jarillo-Herrero P and Fu L 2023 Magic-angle helical trilayer graphene *Sci. Adv.* **9** eaid6063
[19] Kapfer M *et al* 2023 Programming twist angle and strain profiles in 2d materials *Science* **381** 677–81
[20] Li Y *et al* 2022 Symmetry breaking and anomalous conductivity in a double-moiré superlattice *Nano Lett.* **22** 6215–22
[21] Turkel S *et al* 2022 Orderly disorder in magic-angle twisted trilayer graphene *Science* **376** 193–9
[22] Li Y *et al* 2024 Tuning commensurability in twisted van der waals bilayers *Nature* **625** 494–9
[23] Ahn S J *et al* 2018 Dirac electrons in a dodecagonal graphene quasicrystal *Science* **361** 782–6
[24] Uri A *et al* 2023 Superconductivity and strong interactions in a tunable moiré quasicrystal *Nature* **620** 762–7
[25] Suárez Morell E, Correa J D, Vargas P, Pacheco M and Barticevic Z 2010 Flat bands in slightly twisted bilayer graphene: tight-binding calculations *Phys. Rev.* B **82** 121407
[26] Gonzalez-Arraga L A, Lado J L, Guinea F and San-Jose P 2017 Electrically controllable magnetism in twisted bilayer graphene *Phys. Rev. Lett.* **119** 107201
[27] Long M, Pantaleón P A, Zhan Z, Guinea F, Silva-Guillén J A and Yuan S 2022 An atomistic approach for the structural and electronic properties of twisted bilayer graphene-boron nitride heterostructures *npj Comput. Mater.* **8** 73
[28] Julku A, Peltonen T J, Liang L, Heikkilä T T and Törmä P 2020 Superfluid weight and berezinskii-kosterlitz-thouless transition temperature of twisted bilayer graphene *Phys. Rev.* B **101** 060505
[29] Sboychakov A O, Rakhmanov A L, Rozhkov A V and Nori F 2015 Electronic spectrum of twisted bilayer graphene *Phys. Rev.* B **92** 075402
[30] Ramires A and Lado J L 2021 Emulating heavy fermions in twisted trilayer graphene *Phys. Rev. Lett.* **127** 026401
[31] Baldo L, Löthman T, Holmvall P and Black-Schaffer A M 2023 Defect-induced band restructuring and length scales in twisted bilayer graphene *Phys. Rev.* B **108** 125141
[32] Ramzan M S, Goodwin Z A H, Mostofi A A, Kuc A and Lischner J 2023 Effect of coulomb impurities on the electronic structure of magic angle twisted bilayer graphene *npj 2D Mater. Appl.* **7** 49
[33] Ramires A and Lado J L 2018 Electrically tunable gauge fields in tiny-angle twisted bilayer graphene *Phys. Rev. Lett.* **121** 146801
[34] Mao Y, Guerci D and Mora C 2023 Supermoiré low-energy effective theory of twisted trilayer graphene *Phys. Rev.* B **107** 125423
[35] Carr S, Fang S and Kaxiras E 2020 Electronic-structure methods for twisted moiré layers *Nat. Rev. Mater.* **5** 748–63

[36] Orús Rán 2014 A practical introduction to tensor networks: Matrix product states and projected entangled pair states *Ann. Phys., NY* **349** 117–58

[37] Carleo G and Troyer M 2017 Solving the quantum many-body problem with artificial neural networks *Science* **355** 602–6

[38] Cerezo M *et al* 2021 Variational quantum algorithms *Nat. Rev. Phys.* **3** 625–44

[39] Arovas D P, Berg E, Kivelson S A and Raghu S 2022 The hubbard model *Annu. Rev. Condens. Matter Phys.* **13** 239–74

[40] Qin M, Schäfer T, Andergassen S, Corboz P and Gull E 2022 The hubbard model: A computational perspective *Annu. Rev. Condens. Matter Phys.* **13** 275–302

[41] White S R 1992 Density matrix formulation for quantum renormalization groups *Phys. Rev. Lett.* **69** 2863–6

[42] Orús Rán 2019 Tensor networks for complex quantum systems *Nat. Rev. Phys.* **1** 538–50

[43] Schollwöck U 2011 The density-matrix renormalization group in the age of matrix product states *Ann. Phys., NY* **326** 96–192

[44] Haegeman J, Lubich C, Oseledets I, Vandereycken B and Verstraete F 2016 Unifying time evolution and optimization with matrix product states *Phys. Rev.* B **94** 165116

[45] Schollwöck U 2005 The density-matrix renormalization group *Rev. Mod. Phys.* **77** 259–315

[46] Cirac J I, Pérez-García D, Schuch N and Verstraete F 2021 Matrix product states and projected entangled pair states: Concepts, symmetries, theorems *Rev. Mod. Phys.* **93** 045003

[47] Fishman M, White S R and Stoudenmire E M 2022 The ITensor software library for tensor network calculations *SciPost Phys. Codebases* 4

[48] Zheng B-X, Chung C-M, Corboz P, Ehlers G, Qin M-P, Noack R M, Shi H, White S R, Zhang S and Chan G K-L 2017 Stripe order in the underdoped region of the two-dimensional hubbard model *Science* **358** 1155–60

[49] Marten S, Bollmark G, Köhler T, Manmana S R and Kantian A 2023 Transient superconductivity in three-dimensional Hubbard systems by combining matrix-product states and self-consistent mean-field theory *SciPost Phys.* **15** 236

[50] Bollmark G, Köhler T, Pizzino L, Yang Y, Hofmann J S, Shi H, Zhang S, Giamarchi T and Kantian A 2023 Solving 2d and 3d lattice models of correlated fermions—combining matrix product states with mean-field theory *Phys. Rev. X* **13** 011039

[51] Stoudenmire E and Schwab D J 2016 Supervised learning with tensor networks *Advances in Neural Information Processing Systems* vol 29, ed D Lee, M Sugiyama, U Luxburg, I Guyon and R Garnett (Curran Associates, Inc.) (available at: https://proceedings.neurips.cc/paper_files/paper/2016/file/5314b9674c86e3f9d1ba25ef9bb32895-paper.pdf)

[52] Stoudenmire E M 2018 Learning relevant features of data with multi-scale tensor networks *Quantum Sci. Technol.* **3** 034003

[53] Dilip R, Liu Y-J, Smith A and Pollmann F 2022 Data compression for quantum machine learning *Phys. Rev. Res.* **4** 043007

[54] Han Z-Y, Wang J, Fan H, Wang L and Zhang P 2018 Unsupervised generative modeling using matrix product states *Phys. Rev. X* **8** 031012

[55] Bradley T-D, Stoudenmire E M and Terilla J 2020 Modeling sequences with quantum states: a look under the hood *Mach. Learn.: Sci. Technol.* **1** 035008

[56] Cheng S, Wang L, Xiang T and Zhang P 2019 Tree tensor networks for generative modeling *Phys. Rev. B* **99** 155131

[57] Zhou Y, Stoudenmire E M and Waintal X 2020 What limits the simulation of quantum computers? *Phys. Rev. X* **10** 041038

[58] Tindall J, Fishman M, Stoudenmire E M and Sels D 2024 Efficient tensor network simulation of ibm's eagle kicked ising experiment *PRX Quantum* **5** 010308

[59] Niedermeier M, Nairn M, Flindt C and Lado J L 2024 Quantum computing topological invariants of two-dimensional quantum matter (arXiv:2404.06048)

[60] Pan F, Chen K and Zhang P 2022 Solving the sampling problem of the sycamore quantum circuits *Phys. Rev. Lett.* **129** 090502

[61] Pan F and Zhang P 2022 Simulation of quantum circuits using the big-batch tensor network method *Phys. Rev. Lett.* **128** 030501

[62] Niedermeier M, Lado J L and Flindt C 2024 Simulating the quantum fourier transform, grover's algorithm and the quantum counting algorithm with limited entanglement using tensor networks *Phys. Rev. Res.* **6** 033325

[63] Zhang S-X *et al* 2023 Tensorcircuit: a quantum software framework for the nisq era *Quantum* **7** 912

[64] Torlai G and Fishman M 2020 PastaQ: a package for simulation, tomography and analysis of quantum computers (available at: https://github.com/GTorlai/PastaQ.jl/)

[65] Ritter M K, Nú nez Fernández Y, Wallerberger M, von Delft J, Shinaoka H and Waintal X 2024 Quantics tensor cross interpolation for high-resolution parsimonious representations of multivariate functions *Phys. Rev. Lett.* **132** 056501

[66] Shinaoka H, Wallerberger M, Murakami Y, Nogaki K, Sakurai R, Werner P and Kauch A 2023 Multiscale space-time ansatz for correlation functions of quantum systems based on quantics tensor trains *Phys. Rev. X* **13** 021015

[67] Rohshap S, Ritter M K, Shinaoka H, von Delft J, Wallerberger M and Kauch A 2024 Two-particle calculations with quantics tensor trains – solving the parquet equations (arXiv:2410.22975)

[68] Sakaue K, Shinaoka H and Sakurai R 2024 Learning tensor trains from noisy functions with application to quantum simulation (arXiv:2405.12730)

[69] Weiße A, Wellein G, Alvermann A and Fehske H 2006 The kernel polynomial method *Rev. Mod. Phys.* **78** 275–306

[70] Nagai Y, Ota Y and Machida M 2012 Efficient numerical self-consistent mean-field approach for fermionic many-body systems by polynomial expansion on spectral density *J. Phys. Soc. Japan* **81** 024710

[71] Nú nez Fernández Y, Jeannin M, Dumitrescu P T, Kloss T, Kaye J, Parcollet O and Waintal X 2022 Learning feynman diagrams with tensor trains *Phys. Rev. X* **12** 041018

[72] Núñez Fernández Y *et al* 2024 Learning tensor networks with tensor cross interpolation: new algorithms and libraries (arXiv:2407.02454 [physics.comp-ph])

[73] Erpenbeck A *et al* 2023 Tensor train continuous time solver for quantum impurity models *Phys. Rev. B* **107** 245135

[74] Jeannin M, Nú nez Fernández Y, Kloss T, Parcollet O and Waintal X 2024 Cross-extrapolation reconstruction of low-rank functions and application to quantum many-body observables in the strong coupling regime *Phys. Rev. B* **110** 035124

[75] Jolly N, Núñez Fernández Y and Waintal X 2023 Tensorized orbitals for computational chemistry (arXiv:2308.03508)

[76] Murray M, Shinaoka H and Werner P 2024 Nonequilibrium diagrammatic many-body simulations with quantics tensor trains *Phys. Rev. B* **109** 165135

[77] Wang P, Zheng Y, Chen X, Huang C, Kartashov Y V, Torner L, Konotop V V and Ye F 2019 Localization and delocalization of light in photonic moiré lattices *Nature* **577** 42–46

[78] Fu Q, Wang P, Huang C, Kartashov Y V, Torner L, Konotop V V and Ye F 2020 Optical soliton formation controlled by angle twisting in photonic moiré lattices *Nat. Photon.* **14** 663–8

[79] Caha I *et al* 2024 Magnetic single wall CrI3 nanotubes encapsulated within multiwall Carbon Nanotubes (arXiv:2405.14967 [cond-mat.mtrl-sci])

[80] pyqula library (available at: https://github.com/joselado/pyqula)

[81] qtcipy library (available at: https://github.com/joselado/qtcipy)

[82] Mao J *et al* 2020 Evidence of flat bands and correlated states in buckled graphene superlattices *Nature* **584** 215–20

[83] Manesco A L R and Lado J L 2021 Correlation-induced valley topology in buckled graphene superlattices *2D Mater.* **8** 035057

[84] Gao Q, Dong J, Ledwith P, Parker D and Khalaf E 2023 Untwisting moire physics: Almost ideal bands and fractional chern insulators in periodically strained monolayer graphene *Phys. Rev. Lett.* **131** 096401

[85] Wan X, Sarkar S, Lin S-Z and Sun K 2023 Topological exact flat bands in two-dimensional materials under periodic strain *Phys. Rev. Lett.* **130** 216401

[86] Phong V T and Mele E J 2022 Boundary modes from periodic magnetic and pseudomagnetic fields in graphene *Phys. Rev. Lett.* **128** 176406

[87] Nakatsuji N, Kawakami T and Koshino M 2023 Multiscale lattice relaxation in general twisted trilayer graphenes *Phys. Rev. X* **13** 041007

[88] Craig I M, Van Winkle M, Groschner C, Zhang K, Dowlatshahi N, Zhu Z, Taniguchi T, Watanabe K, Griffin S M and Bediako D K 2024 Local atomic stacking and symmetry in twisted graphene trilayers *Nat. Mater.* **23** 323–30

[89] Engelke R *et al* 2023 Topological nature of dislocation networks in two-dimensional moiré materials *Phys. Rev. B* **107** 125413

[90] Kreutzer M, Pieper A, Hager G, Wellein G, Alvermann A and Fehske H 2015 Performance engineering of the kernel polynomal method on large-scale cpu-gpu systems *2015 IEEE Int. Parallel and Distributed Processing Symp.* vol 78 (IEEE) pp 417–26

[91] Kronik L, Makmal A, Tiago M L, Alemany M M G, Jain M, Huang X, Saad Y and Chelikowsky J R 2006 Parsec—the pseudopotential algorithm for real-space electronic structure calculations: recent advances and novel applications to nano-structures *Phys. Status Solidi* b **243** 1063–79

[92] Prentice J C A *et al* 2020 The onetep linear-scaling density functional theory program *J. Chem. Phys.* **152** 174111

[93] Ivanov A V, Levi G, Jónsson E O and Jónsson H 2021 Method for calculating excited electronic states using density functionals and direct orbital optimization with real space grid or plane-wave basis set *J. Chem. Theory Comput.* **17** 5034–49

[94] Mortensen J J *et al* 2024 Gpaw: an open python package for electronic structure calculations *J. Chem. Phys.* **160** 092503

[95] Soler J M, Artacho E, Gale J D, García A, Junquera J, Ordejón P and Sánchez-Portal D 2002 The siesta method for ab initio order-n materials simulation *J. Phys.: Condens. Matter* **14** 2745–79

[96] Park G, Son S, Kim J, Chang Y, Zhang K, Kim M, Lee J and Park J-G 2024 New twisted van der waals fabrication method based on strongly adhesive polymer *2D Mater.* **11** 025021

[97] Son S *et al* 2020 Strongly adhesive dry transfer technique for van der waals heterostructure *2D Mater.* **7** 041005

[98] Nuckolls K P *et al* 2023 Quantum textures of the many-body wavefunctions in magic-angle graphene *Nature* **620** 525–32

[99] Nuckolls K P and Yazdani A 2024 A microscopic perspective on moiré materials *Nat. Rev. Mater.* **9** 460–80

[100] Kim H, Choi Y, Lewandowski C, Thomson A, Zhang Y, Polski R, Watanabe K, Taniguchi T, Alicea J and Nadj-Perge S 2022 Evidence for unconventional superconductivity in twisted trilayer graphene *Nature* **606** 494–500

[101] Frano A *et al* 2016 Long-range charge-density-wave proximity effect at cuprate/manganate interfaces *Nat. Mater.* **15** 831–34

[102] Miao H *et al* 2019 Formation of incommensurate charge density waves in cuprates *Phys. Rev. X* **9** 031042

[103] Fleming R M, Moncton D E, McWhan D B and DiSalvo F J 1980 Broken hexagonal symmetry in the incommensurate charge-density wave structure of 2h-tase$_2$ *Phys. Rev. Lett.* **45** 576–9

[104] Yan S, Iaia D, Morosan E, Fradkin E, Abbamonte P and Madhavan V 2017 Influence of domain walls in the incommensurate charge density wave state of cu intercalated 1t — tise$_2$ *Phys. Rev. Lett.* **118** 106405

[105] Fang A, Ru N, Fisher I R and Kapitulnik A 2007 Stm studies of tbte$_3$: Evidence for a fully incommensurate charge density wave *Phys. Rev. Lett.* **99** 046401